Edge profile analysis of Joint European Torus (JET) Thomson scattering data: Quantifying the systematic error due to edge localised mode synchronisation

M. J. Leyland, M. N. A. Beurskens, J. C. Flanagan, L. Frassinetti, K. J. Gibson, M. Kempenaars, M. Maslov, R. Scannell, and

Citation: Review of Scientific Instruments **87**, 013507 (2016);
View online: https://doi.org/10.1063/1.4939855
View Table of Contents: http://aip.scitation.org/toc/rsi/87/1
Published by the American Institute of Physics

REVIEW OF SCIENTIFIC INSTRUMENTS **87**, 013507 (2016)

Edge profile analysis of Joint European Torus (JET) Thomson scattering data: Quantifying the systematic error due to edge localised mode synchronisation

M. J. Leyland,[1,2,a)] M. N. A. Beurskens,[3] J. C. Flanagan,[2] L. Frassinetti,[4] K. J. Gibson,[1] M. Kempenaars,[2] M. Maslov,[2] R. Scannell,[2] and JET Contributors[b)]
EUROfusion Consortium, JET, Culham Science Centre, Abingdon OX14 3DB, United Kingdom
[1]*Department of Physics, York Plasma Institute, University of York, Heslington, York YO10 5DD, United Kingdom*
[2]*CCFE, Culham Science Centre, Abingdon, Oxfordshire OX14 3DB, United Kingdom*
[3]*Max-Planck Institute für Plasma Physik, D-17491 Greifswald, Germany*
[4]*Division of Fusion Plasma Physics, KTH, SE-10044 Stockholm, Sweden*

(Received 21 September 2015; accepted 19 December 2015; published online 22 January 2016)

The Joint European Torus (JET) high resolution Thomson scattering (HRTS) system measures radial electron temperature and density profiles. One of the key capabilities of this diagnostic is measuring the steep pressure gradient, termed the pedestal, at the edge of JET plasmas. The pedestal is susceptible to limiting instabilities, such as Edge Localised Modes (ELMs), characterised by a periodic collapse of the steep gradient region. A common method to extract the pedestal width, gradient, and height, used on numerous machines, is by performing a modified hyperbolic tangent (mtanh) fit to overlaid profiles selected from the same region of the ELM cycle. This process of overlaying profiles, termed ELM synchronisation, maximises the number of data points defining the pedestal region for a given phase of the ELM cycle. When fitting to HRTS profiles, it is necessary to incorporate the diagnostic radial instrument function, particularly important when considering the pedestal width. A deconvolved fit is determined by a forward convolution method requiring knowledge of only the instrument function and profiles. The systematic error due to the deconvolution technique incorporated into the JET pedestal fitting tool has been documented by Frassinetti *et al.* [Rev. Sci. Instrum. **83**, 013506 (2012)]. This paper seeks to understand and quantify the systematic error introduced to the pedestal width due to ELM synchronisation. Synthetic profiles, generated with error bars and point-to-point variation characteristic of real HRTS profiles, are used to evaluate the deviation from the underlying pedestal width. We find on JET that the ELM synchronisation systematic error is negligible in comparison to the statistical error when assuming ten overlaid profiles (typical for a pre-ELM fit to HRTS profiles). This confirms that fitting a mtanh to ELM synchronised profiles is a robust and practical technique for extracting the pedestal structure. [http://dx.doi.org/10.1063/1.4939855]

I. INTRODUCTION

The steep pressure gradient region at the edge of a tokamak plasma in high confinement mode (H-mode) is termed as the pedestal. The relatively high edge pressures obtained due to the formation of a pedestal are highly desirable as it has been shown that the pedestal height is strongly linked to plasma core performance.[1] However, the pedestal is also prone to limiting instabilities such as edge localised modes (ELMs).[2] ELMs are a periodic collapse of the pedestal due to reaching a critical width and height, thought to be associated with crossing the peeling-ballooning boundary.[3] It is important to be able to accurately quantify the pedestal structure to help understand the underlying physical mechanisms governing the pedestal formation and associated limits.

On the Joint European Torus (JET), radial electron temperature and density profiles, with sufficient spatial resolution to resolve the pedestal width, are provided by the high resolution Thomson scattering (HRTS) system.[4] More specifically, the full width half maximum (FWHM) of the HRTS instrument function in the pedestal region is ≈1.0 cm,[5] which is less than the minimum pedestal width seen on JET, ≈1.5 cm.[6–10] A JET HRTS profile consists of 63 spatial points spanning from the plasma core at ≈3.0 m to the plasma edge at ≈3.9 m. There are typically two to three spatial points defining the pedestal region. The HRTS laser fires every 50 ms, and assuming the ELM period varies between ≈25 and 150 ms[9] for a typical type I ELMy H-mode, on average there are one to two profiles per ELM period.

When investigating the pedestal, it is important to accurately quantify the pedestal structure. This can be achieved by maximising the number of points defining the pedestal by overlaying profiles from the same phase of the ELM cycle (referred to as ELM synchronisation). The resulting combination of profiles is referred to as a composite profile. A modified

a)Email: matthew.leyland@york.ac.uk
b)See the Appendix of Romanelli *et al.*, in Proceedings of the 25th IAEA Fusion Energy Conference, Saint Petersburg, Russia, 2014.

hyperbolic tangent (mtanh) function is fitted to this composite profile to extract the pedestal width, gradient, and height.[11] This is a common technique used on many machines such as JET,[6] AUG,[12,13] DIII-D,[14,15] Alcator C-Mod,[16,17] MAST,[18–21] NSTX,[22] and JT-60.[23] Typically, on JET, HRTS profiles within the last 70%–99% of the ELM cycle (from a window spanning the stationary phase of a pulse, typically ≈2 s) are used to determine pre-ELM fits.[5,6]

The JET HRTS instrument function is calculated numerically using knowledge of the geometrical layout of the laser beam, collection optics, and the orientation of the magnetic flux surfaces in the pedestal region.[5] The instrument function is not used to directly deconvolve the temperature and density profiles due to the potential of introducing artifacts. Instead, the pedestal fitting routine determines a deconvolved mtanh fit using a forward convolution technique requiring knowledge of only the profiles and instrument function. This deconvolution technique, termed classic in the context of Frassinetti *et al.*[5] and Scannell *et al.*,[24] works well for the density profiles. However, for the temperature profiles, it is necessary to weight them by the density profiles. This is to account for the variation in density across the scattering volume corresponding to a single spatial point. This technique is termed weighted deconvolution.[24]

In the current HRTS system configuration (where the instrument function FWHM ≈11 mm), it has been shown that the systematic error introduced to the pedestal width by the deconvolution techniques is negligible (<1%) and below the statistical error for widths above ≈22 mm.[5,24] The statistical error is typically on average ≈3%–5% although this varies with the number of profiles used in the fit, as quantified in this paper. As the density pedestal width decreases to approach the FWHM, the classic deconvolution systematic error increases up to 5%. Whereas for the temperature pedestal width, the weighted deconvolution systematic error increases up to 10%. The FWHM is the minimum measurable pedestal width.

Another source of systematic error, when performing a mtanh fit, arises from ELM synchronisation of the HRTS profiles. When overlaying the profiles, the radial position of each profile is shifted relative to the plasma edge as determined by the magnetic equilibrium reconstruction. This shift accounts for any change in profile position during the ELM cycle so that the steep gradient region of the profiles accurately overlays. However, uncertainty in the plasma edge position, due to small scale plasma movements or any error in the magnetic equilibrium reconstruction, will result in a misalignment of the profiles. This will introduce a systematic error to the mtanh fit parameters.

This paper presents a method, which requires knowledge of the JET HRTS system, to quantify the systematic error due to ELM synchronisation on the pedestal width. Section II provides an overview of the HRTS system. Section III describes the process of generating synthetic HRTS profiles from known underlying temperature and density profiles. More specifically, to replicate the point-to-point variation of a HRTS profile, Section III simulates a HRTS polychromator by (i) estimating the photon throughput of the HRTS system using Raman calibration measurements, (ii) using this to correct an estimate for the number of Thomson scattered photons at a given temperature and density, (iii) distributing these Thomson scattered photons into the polychromator wavelength bands (channels), (iv) adding noise to each channel characteristic of the HRTS system, and (v) fitting to the channel response to determine a synthetic measured temperature and density. Section IV presents the results from replicating fitting to ELM synchronised synthetic HRTS profiles so as to quantify the deviation of the mtanh fit from the underlying profile. Section V presents the conclusions.

II. OVERVIEW OF HRTS SYSTEM

The HRTS system was installed in 2005 and started routine operation in 2007. This system complements the two other Thomson scattering systems on JET, the main and edge light detection and ranging (LIDAR) systems which produce profiles by means of a time-of-flight method.[25] In addition, other complementary kinetic radial profile diagnostics on JET include Li-beam,[26] reflectometry,[27] and electron cyclotron emission[28] systems. The HRTS system has been previously described by Pasqualotto *et al.*[4] and Frassinetti *et al.*[5] in varying levels of detail. Improvements to the system have been made since it was first installed. This section describes, in detail, the current system configuration focusing on the aspects pertinent to this paper.

The HRTS system uses a 5 J Q-switched linearly polarised Nd:YAG laser (λ = 1064 nm) with a 20 ns pulse duration and a 20 Hz repetition rate throughout the JET pulse (≈800 profiles). This custom built laser is situated in the roof laboratory above the torus hall. The laser beam is directed down into the torus hall and then horizontally into the vessel at a beam dump on the inner wall. The resulting Thomson scattered light is collected by a large diameter lens in a vertical port at 90° to the path of the laser beam. This lens images the scattered light from the laser chord within the vessel onto an array of 150 parabolic mirrors. Each mirror couples the scattered light into a 1 mm core optical fibre. These fibres lead to a bank of 21 polychromators, situated outside the biological shielding surrounding the torus hall. The arrival of the scattered light from the torus hall to the polychromators is staggered by varying the length of optical fibre. This allows one polychromator to measure the scattered spectrum for multiple spatial points, in this case three. This technique is referred to as multiplexing, and consequently, a full HRTS radial profile has 63 spatial points.

There are two possible lines-of-sight for the HRTS system corresponding to two different beam dumps on the inner wall. During JET operations with the carbon wall (JET-C), after the installation of HRTS, the upper beam dump was a carbon plate only sufficient, in terms of power handling, for the LIDAR laser, whereas the lower beam dump was a higher specification knife edge beam dump made from Inconel steel. The HRTS system required the knife edge beam dump and, therefore, was configured to the lower line of sight for all JET-C plasmas. As shown in Figure 1, the lower line of sight (blue) for a high triangularity ELMy H-mode typically passes below the central axis. While the profiles can be mapped onto the mid-plane, it is not possible to measure the peak core density and temperature for this configuration.

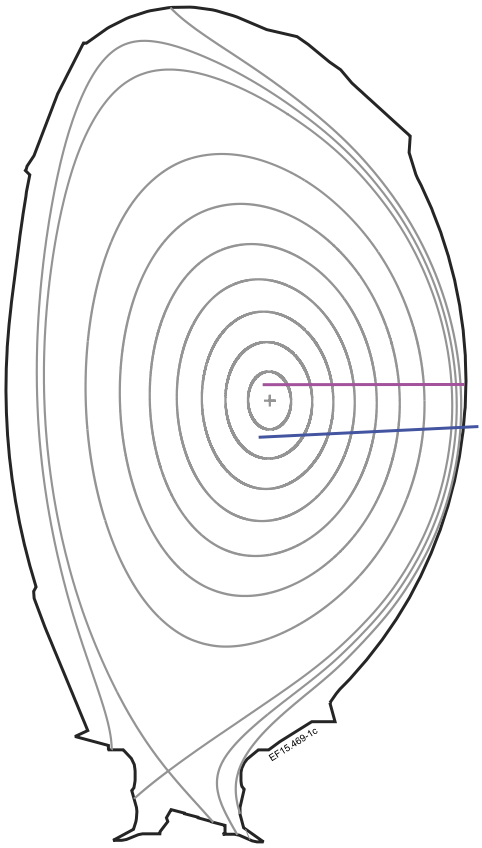

FIG. 1. Magnetic equilibrium reconstruction for JET pulse number 79503 (JET-C plasma) at t ≈ 22.0 s showing the lower (magenta) HRTS line-of-sight. The upper HRTS line-of-sight is also shown, in blue, as used for the first JET-ILW campaign.

The upper beam dump was upgraded to a knife edge variant during the installation of the ITER-Like-Wall (ILW), and for the subsequent campaign period, HRTS was switched to the upper line of sight. Figure 1 shows that the upper line of sight (magenta) is typically closer to the plasma core for a high triangularity ELMy H-mode. However, since the first JET-ILW campaign, the HRTS system has been configured back onto the lower line of sight as the view of the edge region is better (less vignetting). This results in higher quality edge measurements.

The HRTS polychromators separate the Thomson scattered signal into four wavelength bands (channels) using interference filters. The signal strength of each channel is measured by an avalanche photo diode (APD). These four signals are used to determine the temperature and density for a spatial point along the radial profile. In principle, the absolute height of each channel indicates the density, and the relative height of each channel indicates the temperature. In practice, the HRTS system uses a least squares minimisation technique to compare the channel intensities with a pre-determined table of intensities, calculated with the Selden-Naito expression.[29]

III. GENERATING A SYNTHETIC HRTS PROFILE

This study considers synthetic HRTS profiles to quantify the systematic error due to ELM synchronisation as the underlying profile is known, and therefore, the deviation of the fit from the underlying profile can be evaluated. This section details how knowledge of the HRTS system can be used to generate profiles with noise and error bars representative of real measured HRTS profiles.

A. Number of Thomson scattered photons

The number of Thomson scattered photons collected by the HRTS system is given by Beurskens *et al.*[30] and Scannell *et al.*[31]

$$N_{ph,scat} = n_e \cdot \frac{E_{laser}}{h\upsilon_0} \cdot \frac{d\sigma_{TS}}{d\Omega} \cdot \Delta L \cdot \Delta\Omega \cdot T_{sys} \cdot T_{N,vig}(r) \cdot EQE, \quad (1)$$

where n_e is the electron density, E_{laser} is the laser energy (5 J), $h\nu_0$ is the energy of a photon (1.9×10^{-19} J), $E_{laser}/h\nu_0$ is the total number of photons in a single laser pulse, ΔL is the scattering length (12 mm or 20 mm depending on whether single or double fibre configuration is used corresponding to the edge (R ≈ 3.70–3.90 m) and core (R ≈ 3.00 − 3.70 m), respectively[5]), $\Delta\Omega$ is the solid angle of collection optics ($\approx 2.2 \times 10^{-3}$ sr), $d\sigma_{TS}/d\Omega$ is the Thomson scattering cross section ($= r_0^2 \approx 8.0 \times 10^{-30}$ m^2), T_{sys} is the system transmission, $T_{N,vig}(r)$ is the normalised spatial variation in transmission due to the system vignetting, and EQE is the effective quantum efficiency of the APDs within the polychromators.

The system transmission can be broken down into seven components,

$$T_{sys} = T_{laser} \cdot T_{port} \cdot T_{window} \cdot T_{lens} \cdot T_{mirrors} \cdot T_{fibres} \cdot T_{filters}, \quad (2)$$

where each component is defined in Table I. The wavelength averaged total system transmission is $T_{sys} \approx 0.19$. In addition, the normalised spatially dependent vignetting transmission coefficient $T_{N,vig}(r)$ is evaluated via performing a Raman calibration. This calibration is described in Sec. III B.

B. Raman calibration

As summarised in Scannell[31] Raman scattering is the inelastic scattering of electromagnetic radiation off a molecule resulting in scattered light at discrete wavelengths about the incident laser wavelength (λ_L). The change in scattered photon wavelength and energy corresponds to a change in the rotational (or vibrational) state of the scattering molecule. A molecule that loses energy results in a higher energy, lower wavelength scattered photon with corresponding Raman lines

TABLE I. Components of HRTS optical transmission.

Symbol	Value	Transmission of component
T_{laser}	0.65	Laser
T_{port}	0.70	Vessel port aperture
T_{window}	0.96^4	Vacuum windows (two doublets)
T_{lens}	0.99	Lens (AR coated, mean over 670-1100 nm)
$T_{mirrors}$	0.85^3	Al mirrors (three)
T_{fibres}	0.60	1 mm core pure silica fibre (NA = 0.37)
$T_{filters}$	0.80	Dielectric filters

below λ_L referred to as anti-Stokes lines. Raman lines above λ_L are referred to as Stokes lines and correspond to the scattered photons having relinquished energy to the scattering molecule.

The spectral channels of the HRTS polychromators are designed to detect blue-shifted wavelengths and, consequently, the system can only detect anti-Stokes lines. At the temperatures at which this calibration is performed (300-500 K), signal is seen only in the few channels closest to the laser wavelength. Figure 2 shows the Raman spectra in relation to (a) channel 4 for an edge HRTS polychromator and (b) channel 1 for a core HRTS polychromator. Note that the channel numbering for an edge polychromator is reversed in comparison to that of a core polychromator (see Figure 7). Channel 4 for an edge polychromator is closer to the laser wavelength in comparison to channel 1 for a core polychromator, and therefore, it collects more of the anti-Stokes scattered Raman signal. Consequently, the measured Raman signal is larger for an edge polychromator despite the spectral width of its first channel being narrower in comparison to that of a core polychromator and the smaller scattering length for an edge polychromator (≈12 mm in comparison to ≈20 mm for a core polychromator). Furthermore, the Raman signal for edge polychromators is further reduced for the spatial points affected by vignetting.

Typically, on JET, the vessel is filled with nitrogen gas ranging from 0 to 400 mbar at room temperature (≈20 °C) for a Raman calibration. The gas pressure is constant throughout the vessel resulting in the same number of Raman scattered photons per scattering volume across the HRTS line-of-sight. The difference in measured Raman intensity across the HRTS line of sight, thus, quantifies the differences in coupling and transmission for each light path.[32] It is noted that there is a disparity in system throughput at the plasma edge between Raman calibration measurements made at 20 °C and at the vessel operating temperature of 200 °C. A probable explanation is due to the thermal expansion of the vessel. As described in Section II, the HRTS collection lens is situated in a vertical port at a 90° angle to the laser line-of-sight. It is thought that the position of this vertical port shifts due to thermal expansion improving the view of the plasma edge (reducing the vignetting in this region). Currently, there is not a complete set of Raman measurements at 200 °C for both HRTS lines-of-sight. Furthermore, the existing measurements at this vessel temperature require further analysis. This paper only considers Raman measurements at 20 °C.

Figure 3 shows the normalised spatially dependent transmission coefficient $T_{N,vig}(r)$ for the upper and lower lines of sight mapped onto the magnetic mid-plane. $T_{N,vig}(r)$ is curved for both lines of sight with a maximum at $R_{mid} \approx 3.35$ m due to vignetting of the collection optics field of view by the vertical port. The vignetting is most prominent at the plasma edge where the vertical port significantly obstructs the collection optics field of view. Comparing the upper and lower transmission curves, it can be seen that fewer spatial points are impaired for the lower line of sight.

At the top of the pedestal ($R_{mid} \approx 3.77$ m for JET pulse number 82814), $T_{N,vig} \approx 0.65$. Evaluating Equation (1) results in ≈840 Thomson scattered photons per 10^{19} electrons m^{-3}, assuming a scattering length of 0.012 m and EQE ≈0.2. The expected number of Thomson scattered photons can be verified by further consideration of the signal-to-noise ratio of the Raman calibration data, as detailed in the following.

Figure 4 shows the Raman signal intensity as measured by HRTS polychromator C throughout a Raman calibration JET pulse. The HRTS laser starts firing before t = 0 s as, during normal plasma operation, this is required to obtain stray light measurements before the formation of a plasma. The Raman signal is proportional to the gas pressure, as can be seen by the data in Figure 4. The data in Figure 4 also demonstrate that there is a variation in Raman intensity across the 800 laser pulses. The Raman calibration data for a range of pressures are summarised in Figure 5, which shows the average Raman signal as a function of nitrogen gas pressure where the ordinate error bar is the standard deviation of the Raman signal. Furthermore, Figure 5 demonstrates the linearity (increase in signal with pressure) incorporating multiple Raman JET pulses. The difference in the slope of the dashed lines shown in Figure 5 is due to a variation in system throughput as a

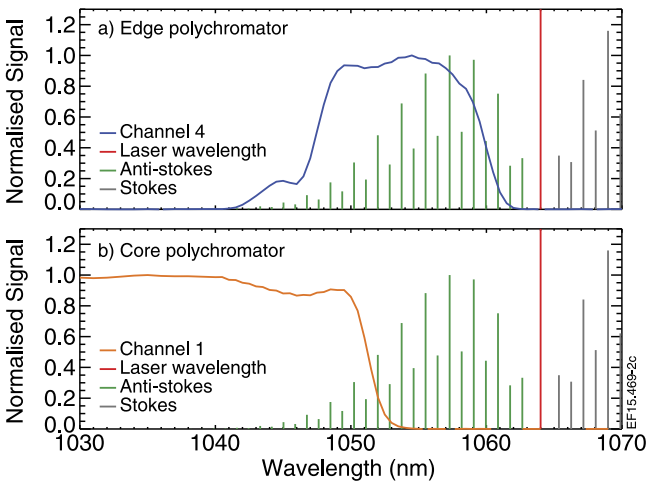

FIG. 2. Raman stokes and antistokes spectra about the HRTS laser wavelength ($\lambda_L = 1064$ nm) together with the spectral response of (a) channel 4 for an edge HRTS polychromator and (b) channel 1 for a core polychromator. The Raman spectra are determined for nitrogen gas and assuming a vessel temperature of 294 K.

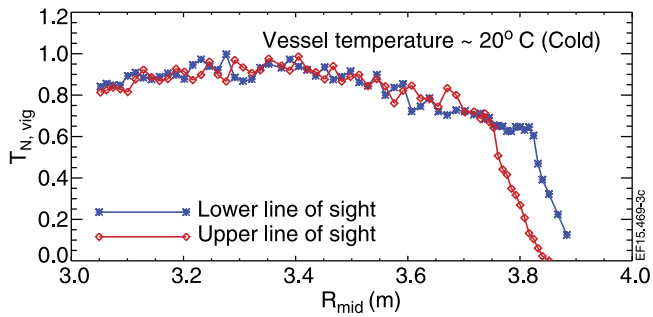

FIG. 3. Transmission curve for the HRTS upper line of sight (red) and lower line of sight (blue) both mapped onto the magnetic mid plane. Mapping performed using magnetic equilibrium reconstruction for JET pulse number 82814 during stationary ELMy H-mode phase. $T_{N,vig}$ determined by variation of Raman scattering intensity across HRTS line of sight when the vessel is filled with nitrogen at 200 mbar. The vessel temperature is at room temperature at ≈294 K (cold).

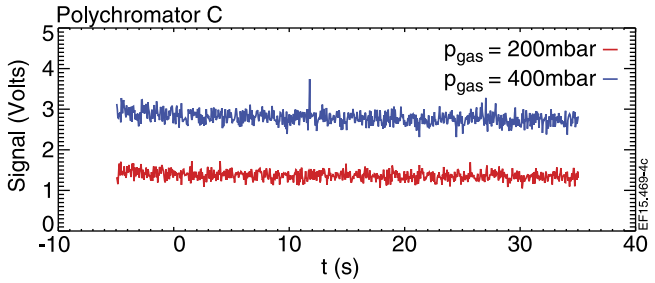

FIG. 4. Raman signal over 800 laser pulses as measured by channel 4 of HRTS polychromator C when the JET vessel is filled with nitrogen gas at 200 mbar (red) and 400 mbar (blue) at $T_{Vessel} \approx 294$ K.

result of independent Raman calibrations at the beginning of each JET campaign and also dependent on the line of sight.

For a high pressure JET Raman pulse (400 mbar), Poisson noise is assumed to be the dominant contribution to the total photon error ($\sigma_{Tot} \approx \sigma_{Poiss} = \sqrt{N}$). In this case, the average Raman signal ($\overline{S}$) and corresponding standard deviation (σ_S) can be used to estimate the number of Raman scattered photons ($N_{Ram,meas}$) as

$$\frac{\sqrt{N_{Ram,meas}}}{N_{Ram,meas}} = \frac{\sigma_S}{\overline{S}}. \quad (3)$$

It is important to note that the values of $\overline{S}$ and σ_S will be inaccurate when the Raman signal is affected by stray light. Consequently, when evaluating $\overline{S}$ and σ_S, the Raman signals suffering from stray light are excluded. This estimate of $N_{Ram,meas}$ can be compared to the number of expected Raman scattered photons ($N_{Ram,calc}$) as calculated using a similar expression to Equation (1) and given by

$$N_{Ram,calc} = \frac{p_{gas}}{k_B T_{vessel}} \cdot \frac{E_{laser}}{h\upsilon_0} \cdot \frac{d\sigma_{Raman}}{d\Omega} \cdot \Delta L \cdot \Delta\Omega \cdot T_{sys} \cdot T_{N,vig}(r) \cdot EQE, \quad (4)$$

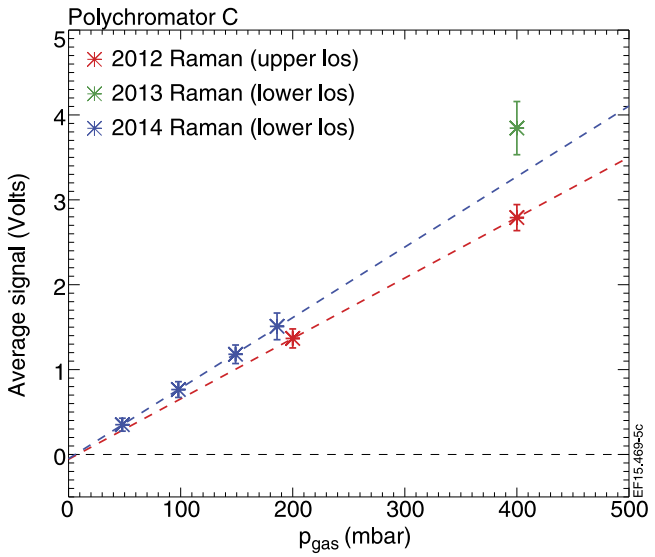

FIG. 5. Raman signal over 800 laser pulses as measured by channel 4 of HRTS polychromator C when the JET vessel is filled with nitrogen gas at 200 mbar (red) and 400 mbar (blue) at $T_{Vessel} \approx 294$ K.

where p_{gas} is the nitrogen gas pressure (40 000 Pa ≡ 400 mbar), k_B is the Boltzmann's constant (1.38×10^{-23} Pa m^3 K^{-1}), T_{vessel} is the temperature of the vessel (≈294 K), $d\sigma_{Raman}/d\Omega$ is the Raman cross section (of the order 1×10^{-35} m^2), and the remaining parameters are as previously defined for Equation (1).

Figure 6(a) compares the calculated (expected) number of Raman scattered photons ($N_{Ram,calc}$) with the measured Raman scattered photons ($N_{Ram,meas}$) for each HRTS spatial point where $N_{Ram,meas} = kN_{Ram,calc}$. The point-to-point variation in the calculated number of photons is due to evaluating $d\sigma_{Raman}/d\Omega$ for each spatial point using the corresponding spectral response and the variation in $T_{N,vig}$, as determined from Raman calibration data for the lower line of sight. As previously described, the step changes in the number of calculated Raman scattered photons ($N_{Ram,calc}$), as shown by Figure 6(a), are due to the changes in scattering length (l_{scat} = 12 mm for single fibre configuration and l_{scat} = 20 mm for double fibre configuration), differences in the overlap between the spectral channel closest to the laser wavelength with the Raman spectra (see Figure 2) and the vignetting curve.

Figures 6(a) and 6(b) compare the measured and calculated number of photons where $k \approx 0.52$ (core) and 0.31 (edge). The discrepancy in the number of photons is likely due to, for example, the crude way that the transmission was estimated. Figure 6(a) also shows, in general, that there is a good relative agreement in the number of Raman scattered photons across the line of sight (apart from for polychromators affected by stray light such as polychromator G corresponding to $R_{mid} \approx 3.68 - 3.72$). This good relative agreement implies that it is correct to assume a Poisson distribution.

To summarise, the measured number of Raman scattered photons is a factor of ≈0.52 (core) and 0.31 (edge) less than expected. This factor is used to correct the number of calculated Thomson scattered photons when generating a synthetic profile.

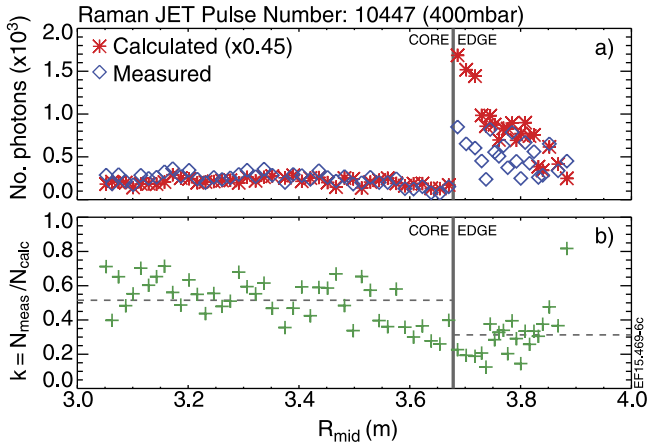

FIG. 6. (a) Comparison of the calculated number of Raman scattered photons ($N_{Ram,calc}$) to the measured number of Raman scattered photons ($N_{Ram,meas}$) for each HRTS spatial point. The number of photons is shown as a function of radial position, mapped onto the midplane corresponding to a typical H-mode plasma. The calculated number of Raman scattered photons for both the core and edge is multiplied by 0.45 in this figure for illustrative purposes only. (b) shows the ratio (green symbols) and average core/edge ratio (horizontal grey dashed line) of the measured to calculated Raman scatter photons ($N_{Ram,meas}/N_{Ram,calc}$).

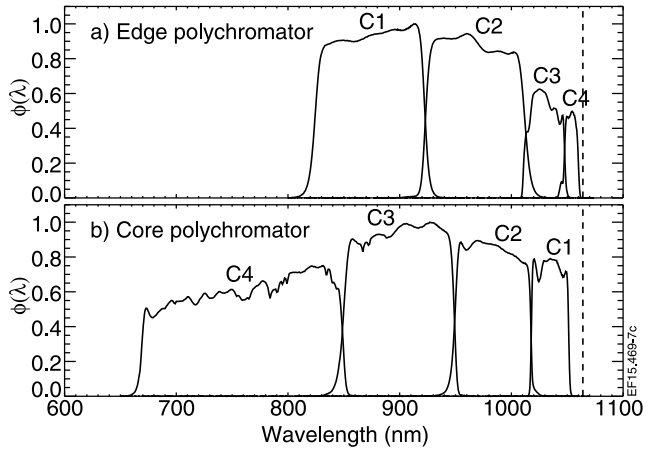

FIG. 7. The normalised spectral response of (a) an edge polychromator (polychromator C, fibre 2) and (b) a core polychromator (polychromator P, fibre 2) relative to the laser wavelength at 1064 nm (black dashed line). Channel 1 (C1) is closest to the laser wavelength for the core polychromator but is furthest away from the laser wavelength for the edge polychromator.

C. Simulating a HRTS polychromator

A HRTS polychromator separates out the total number of scattered photons into four wavelength bands (channels). The response of each channel is dependent on the spectral transmission ($\phi(\lambda)$), the scattered spectrum as given by the Selden-Naito expression ($S(\lambda, \theta, T_e)$), and the quantum efficiency of the photodiodes (for simplicity assume EQE constant for all channels at ≈0.2). The Selden-Naito expression is normalised to unity,[33]

$$S_N(\lambda, \vartheta, T_e) = \int_0^\infty \frac{S(\lambda, \vartheta, T_e)}{\lambda_0} d\lambda = 1, \tag{5}$$

where $S_N(\lambda, \theta, T_e)$ is the normalised Selden-Naito expression. The number of photons detected by each channel (i) is given by integrating the product of the spectral transmission of each polychromator channel $\phi_i(\lambda)$ and the scattered spectrum, as given by

$$N_{ph,dect,chn=i} = N_{ph,scat} \int \phi_i(\lambda) \frac{S(\lambda, \vartheta, T_e)}{\lambda_0} d\lambda. \tag{6}$$

The spectral response for each fibre and polychromator is used when determining the electron temperature and density from HRTS measurements as there is some variation in fibre-to-fibre and polychromator-to-polychromator even though the optical components are nominally identical (due to differences in alignment and high sensitivity of filters to angle of incidence). However, when generating synthetic profiles, a single spectral response is assumed for all edge

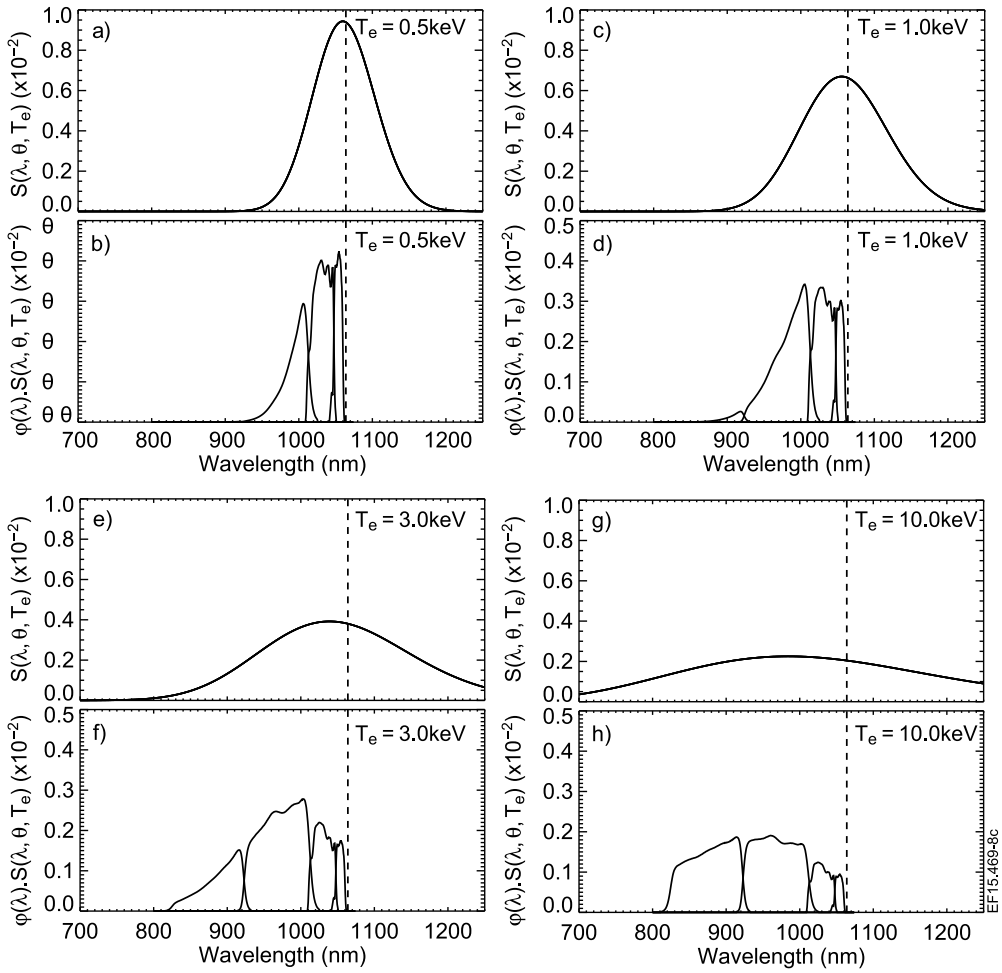

FIG. 8. Scattered Thomson spectrum ($S(\lambda, \theta, T_e)$) for (a) $T_e = 0.5$ keV, (c) $T_e = 1.0$ keV, (e) $T_e = 3.0$ keV, and (g) $T_e = 10.0$ keV. Product of scattered spectrum and the spectral response for an edge polychromator ($\phi(\lambda) \cdot S(\lambda, \theta, T_e)$) for (b) $T_e = 0.5$ keV, (d) $T_e = 1.0$ keV, (f) $T_e = 3.0$ keV, and (h) $T_e = 10.0$ keV where the laser wavelength is 1064 nm (black dashed line).

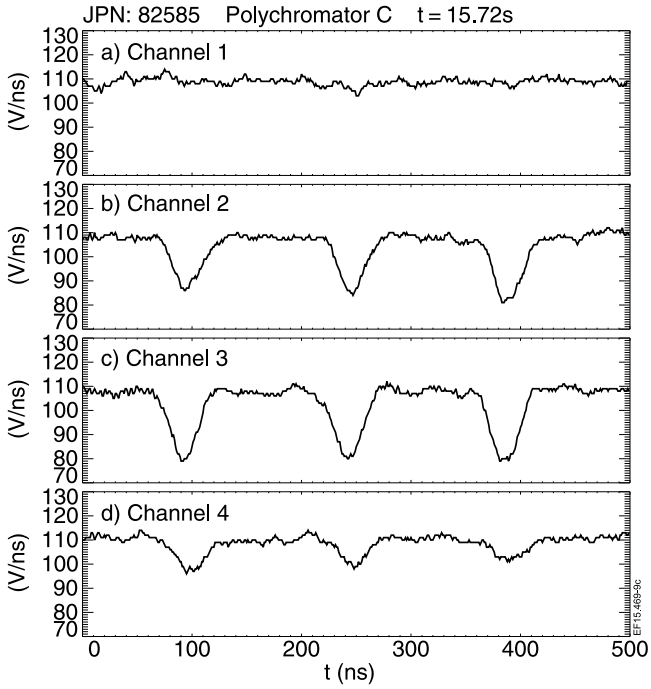

FIG. 9. Measured signal for JET pulse number 82585 for channels 1-4 of polychromator C at t = 15.72 s. Each polychromator measures the signal from three adjacent spatial points due to optical multiplexing by means of delay line fibres.

and core polychromators, for simplicity, as shown by Figures 7(a) and 7(b). The edge polychromators' channels are closer to the laser wavelength, and consequently, the highest wavelength channel is more susceptible to laser stray light. This analysis focuses on the pedestal region, and therefore, the examples below utilise the spectral response of an edge polychromator.

Figure 8 shows the scattered spectrum and the product of the scattered spectrum with the edge polychromator spectral response, as shown in Figure 7(a), for a range of electron temperatures (T_e = 0.5, 1.0, 3.0, and 10.0 keV). Figure 8 demonstrates the change in relative intensities of the polychromator channels as the temperature increases. At higher temperatures, the intensity of lower wavelength channels increases due to the blue shift of the scattered spectrum relative to the laser wavelength.

The number of detected Thomson scattered photons ($N_{ph,dect,chn=i}$) can be expressed as the product of electron density (n_e) and the temperature dependent response of the polychromators ($F_i(T_e)$) given by

$$N_{ph,dect,chn=i} = n_e \cdot F_i(T_e). \tag{7}$$

More specifically, $F_i(T_e)$ details the relative intensity of each channel for a specific temperature and independent of density. Instead of fitting the Selden-Naito expression directly to the signals, it is computationally more efficient in the context of the HRTS system to use a pre-determined table of $F_i(T_e)$ values for a range of electron temperatures. A least squares minimisation technique is used to determine the electron temperature, as shown in Equation (8),

$$\begin{aligned}\chi^2 &= \sum_{i=1-4} w_i \left[N_{ph,dect,chn=i} - n_e \cdot F_i(T_e)\right]^2 \\ &= \sum_{i=1-4} w_i \\ &\quad \times \left[N_{ph,dect,chn=i} - \frac{\sum_{i=1-4} w_i N_{ph,dect,chn=i} F_i}{\sum_{i=1-4} w_i F_i^2} \cdot F_i(T_e)\right]^2,\end{aligned} \tag{8}$$

where $w_i = (\sigma_{N_{ph,dect,chn=i}}/N_{ph,dect,chn=i})^{-2}$ is a weighting factor that results in the least squares minimisation being dominated by the more reliable channels with a relatively low error. The

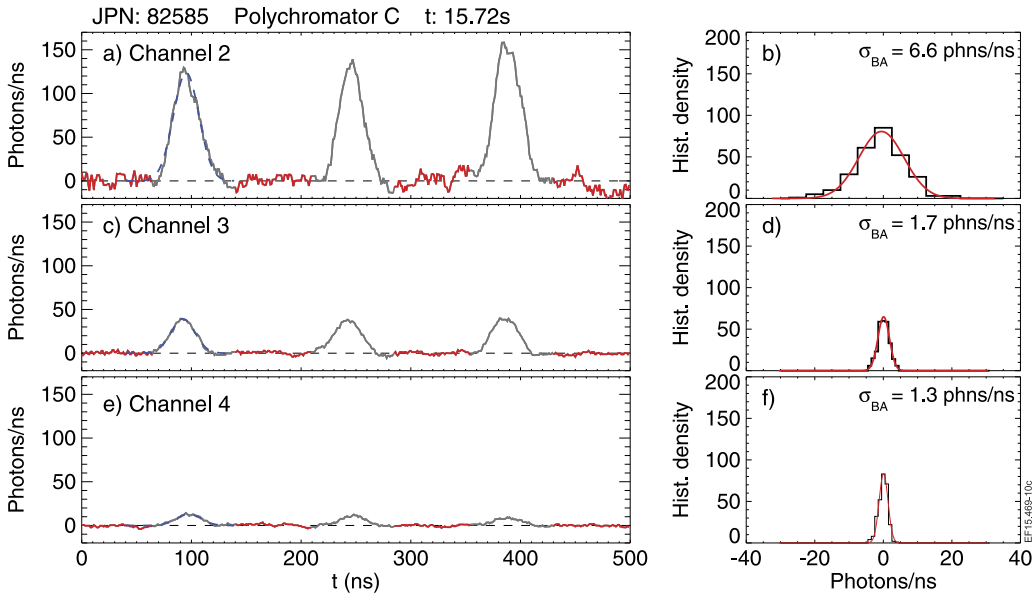

FIG. 10. Measured signal converted into units of photons per ns for JET pulse number 82585 for polychromator C channels (a) 2, (c) 3, and (e) 4 at t = 15.72 s. The number of photons is calculated for each channel at $n_e \approx 5.2\times10^{19}$ m^{-3} and $T_e \approx 0.5\times10^3$ keV using $T_{N,vig} \approx 0.65$ from the cold lower line-of-sight vignetting curve. The blue dashed curves are Gaussian fits to the first Thomson scattering peak in each channel. Histograms of the signal between the Thomson scattering peaks are shown by (b), (d), and (f) along with the corresponding Gaussian fit to quantify the width. Channel 1 is not shown as a negligible number photons are expected in this channel.

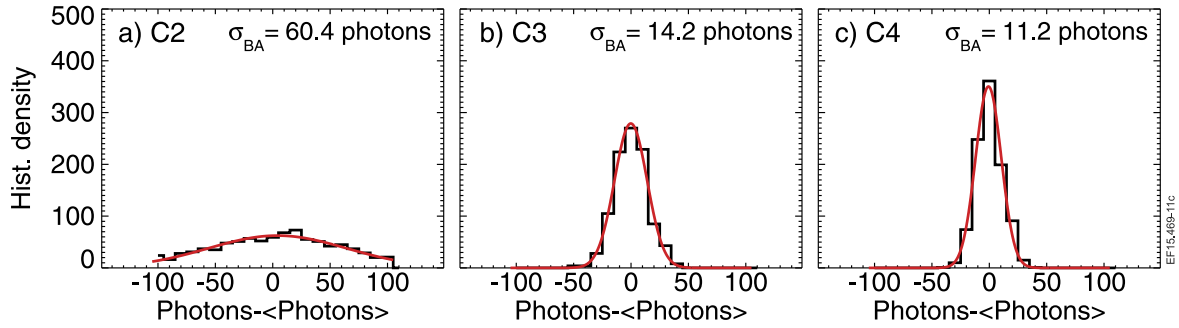

FIG. 11. Histogram of number of photons as determined by applying the characteristic point-to-point noise (Figs. 10(b), 10(d), and 10(f)) to a Gaussian fit to the first Thomson scattering peak of each channel (Figs. 10(a), 10(c), and 10(e)). The integral of the resulting noisy Gaussian is evaluated and the process repeated to build up the histogram. The histogram width is the photon error due to background light and amplifier noise for channels (a) 2, (b) 3, and (c) 4.

electron density is determined by evaluating Equation (9), and F_i values corresponding to the minimum χ^2; the sum of the squared differences,

$$n_e = \frac{\sum_{i=1-4} w_i N_{ph,dect,chn=i} F_i \left(T_{e,min(\chi^2)}\right)}{\sum_{i=1-4} w_i F_i \left(T_{e,min(\chi^2)}\right)^2}. \quad (9)$$

The measured HRTS profiles have a vertical scatter in temperature and density due to the error on the number of photons detected by each channel. More specifically, these errors correspond to a set of F_i values deviating from the underlying F_i (temperature and density). The contributions to the total error in number of detected photons are given by O'Gorman *et al.*[33]

$$\sigma^2_{N,tot} = \sigma^2_{Poisson} + \sigma^2_{background} + \sigma^2_{amplifier}, \quad (10)$$

where $\sigma_{Poisson} = \sqrt{N}$ is the Poisson error. In general, the Poisson distribution quantifies the probability of a number of events, such as photon counts for a given mean. $\sigma_{background}$ is the uncertainty introduced by the background plasma light and $\sigma_{amplifier}$ is the noise introduced by the electronic components. In the Scrape-Off Layer (SOL) region, where there is typically minimal Thomson scattered photons detected, the contribution of $\sigma^2_{Poisson}$ is small in comparison to $\sigma^2_{background} + \sigma^2_{amplifier}$ ($\equiv \sigma^2_{BA}$). To accurately replicate a JET HRTS profile beyond the foot of the pedestal, an estimate for σ_{BA} is required. This is obtained by considering the measured HRTS signal intensity for a single laser pulse.

Figure 9 shows the measured signal intensity for polychromator C, for JET pulse number 82585 at t = 15.72 s. The acquisition time of 500 ns captures three Thomson scattering signals as each polychromator measures three spatial points using delay lines to stagger the signal. For this particular pulse, the first Thomson scattering signal at ≈90 ns corresponds to a spatial point at the top of the pedestal where $n_e \approx 5.2 \times 10^{19}$ m^{-3} and $T_e \approx 0.5$ keV. At this temperature, Figure 9(a) shows that there is no appreciable Thomson scattering signal in channel 1 as expected from Figures 8(a) and 8(b).

The magnitude of the noise between the Thomson scattering signals is a combination of Poisson noise, background plasma light, and a convolution of detector and digitiser response time (~2.0 and 0.7 ns, respectively). To convert the signals shown in Figure 9 into units of photons per ns, a baseline and stray light subtraction is performed centring the signal about zero. The JET HRTS system baseline light level

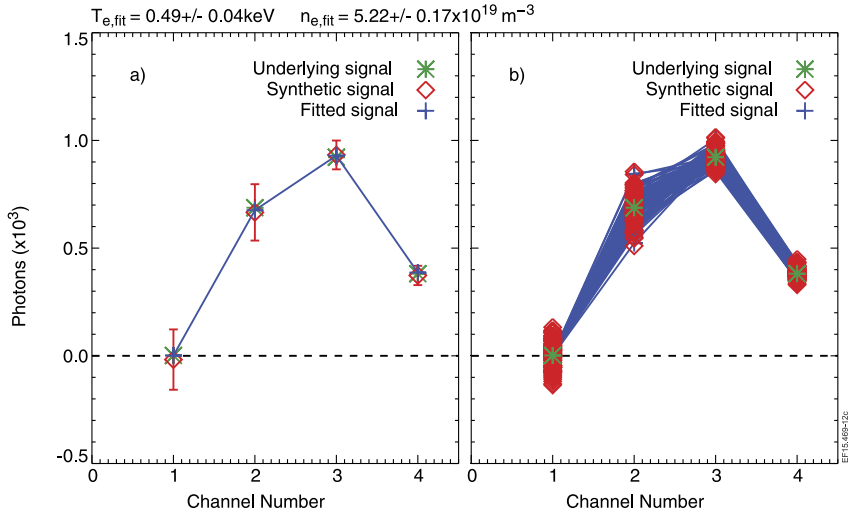

FIG. 12. (a) Example of an underlying signal (green), an underlying signal with noise (also termed synthetic signal) (red) and fitted signal (blue) for an underlying electron density and temperature of $n_e \approx 5.2 \times 10^{19}$ m^{-3} and $T_e \approx 0.5 \times 10^3$ keV, where $T_{N,vig} \approx 0.65$. The resulting fitted electron density and temperature being $n_{e,fit} = 5.22 \pm 0.17 \times 10^{19}$ m^{-3} and $T_{e,fit} = 0.49 \pm 0.04$ keV. (b) The error is determined performing the fit 100 times with different synthetic signals.

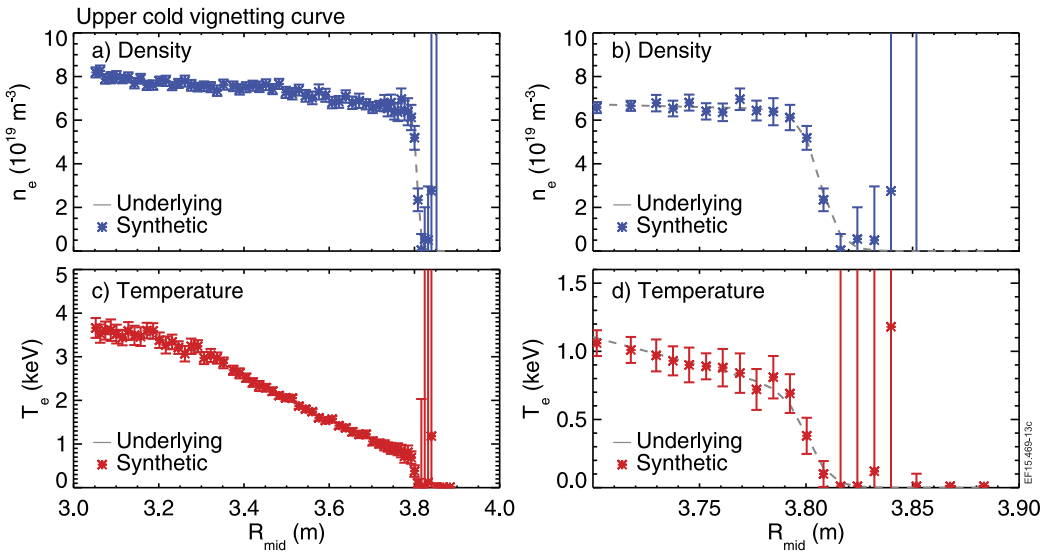

FIG. 13. Underlying (dashed line) and synthetic (asterisk symbol) profiles for electron (a) and (b) density (blue) and (c) and (d) temperature (red). Upper cold vignetting curve incorporated into photon calculation. (a) and (c) show the entire profile, whereas (b) and (d) focus on the pedestal region.

is determined by averaging the 99 laser pulses corresponding to 99 acquisitions before the plasma is formed. In the context of this paper when simulating a HRTS polychromator, since the electron temperature and density are already known from the measured profile, the number of expected photons in each channel can be determined (Equation (1)). This is then used to scale the integral under the peak of the first Thomson scattering signal as shown by Figures 10(a), 10(c), and 10(e).

Figures 10(b), 10(d), and 10(f) show histograms of the signal between the Thomson scattering peaks. The width of each histogram quantifies the point-to-point variation for each channel due to background and amplifier noise in photons per ns. To determine a background and amplifier photon error (σ_{BA}), an integral error, a Monte Carlo technique is used. First, additional noise characteristic of the point-to-point variation is applied to a Gaussian fit to the Thomson scattering peak (dashed blue line shown in Figure 10(a)). Then, the integral under the peak is evaluated to give the number of photons. This process is repeated numerous times to determine the spread in number of photons (σ_{BA}), see Figure 11. The width of the histograms shown by Figure 11 gives the photon error due to background and amplifier noise (σ_{BA}) is 60, 14, and 11 photons for channels 2, 3, and 4, respectively.

The noise between the Thomson scattering peaks increases from channel 4 to 2 (see Figures 10(a),10(c), and 10(e) corresponding to increasing spectral channel width. This suggests that background light is the dominate source of noise as the wider the spectral channel the more background light is collected. Therefore, the photon error for channel 1 can be estimated by scaling according to the spectral width (≈70 photons). The photon errors quoted above have been determined for a spatial point with a single fibre input. For a spatial point with a double fibre input, the scattering length is near doubled and so more background light is collected,

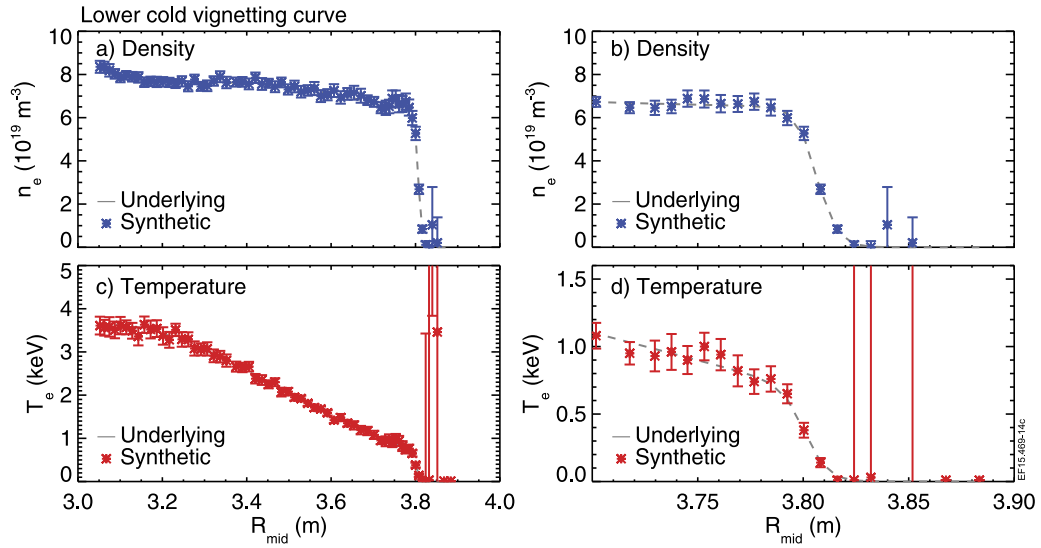

FIG. 14. Underlying (dashed line) and synthetic (asterisk symbol) profiles for electron (a) and (b) density (blue) and (c) and (d) temperature (red). Lower cold vignetting curve incorporated into photon calculation. (a) and (c) show the entire profile, whereas (b) and (d) focus on the pedestal region.

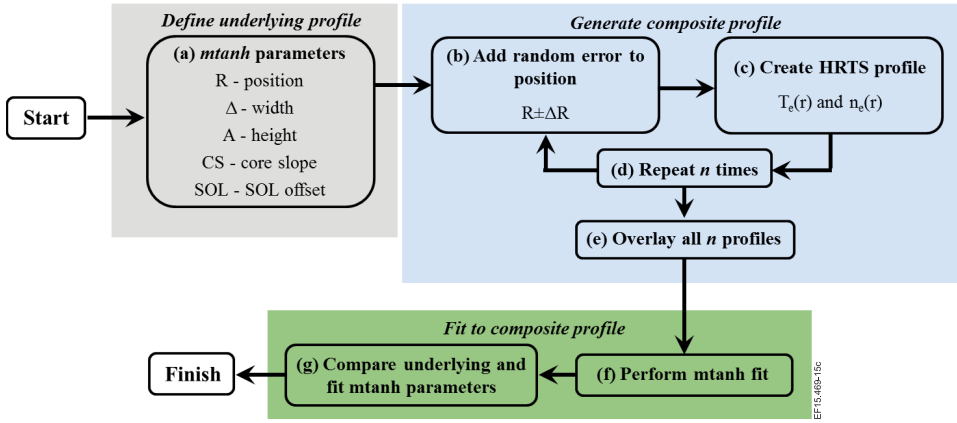

FIG. 15. Schematic of method to access systematic uncertainty introduced by ELM synchronisation. First, an underlying profile is defined (grey). Second, a composite profile is generated consisting of n HRTS like profiles (blue). To finish, a mtanh fit is performed to the composite profile and the difference between the resulting parameters in comparison the original underlying parameters is accessed (green).

resulting in a larger uncertainty. Consequently, for a double fibre input (core polychromators), σ_{BA} is doubled.

Figure 12(a) shows an example of the χ^2 minimisation for a vignetted spatial point near the plasma edge at the top of the pedestal, where the underlying temperature and density are $n_e \approx 5.2 \times 10^{19}$ m^{-3} and $T_e \approx 0.5 \times 10^3$ keV and $T_{N,vig} \approx 0.65$. The underlying signal (green), as inferred from the underlying temperature and density, with the addition of random errors is termed as the synthetic signal (red). The additional error is sampled from a normal distribution of width $\sigma_{N,tot}$. Performing the χ^2 minimisation results in the fitted signal (blue) in Figure 12 corresponding to a temperature and density of $n_{e,fit} = 5.22 \pm 0.17 \times 10^{19}$ m^{-3} and $T_{e,fit} = 0.49 \pm 0.04$ keV. A Monte Carlo technique is used to determine the error of

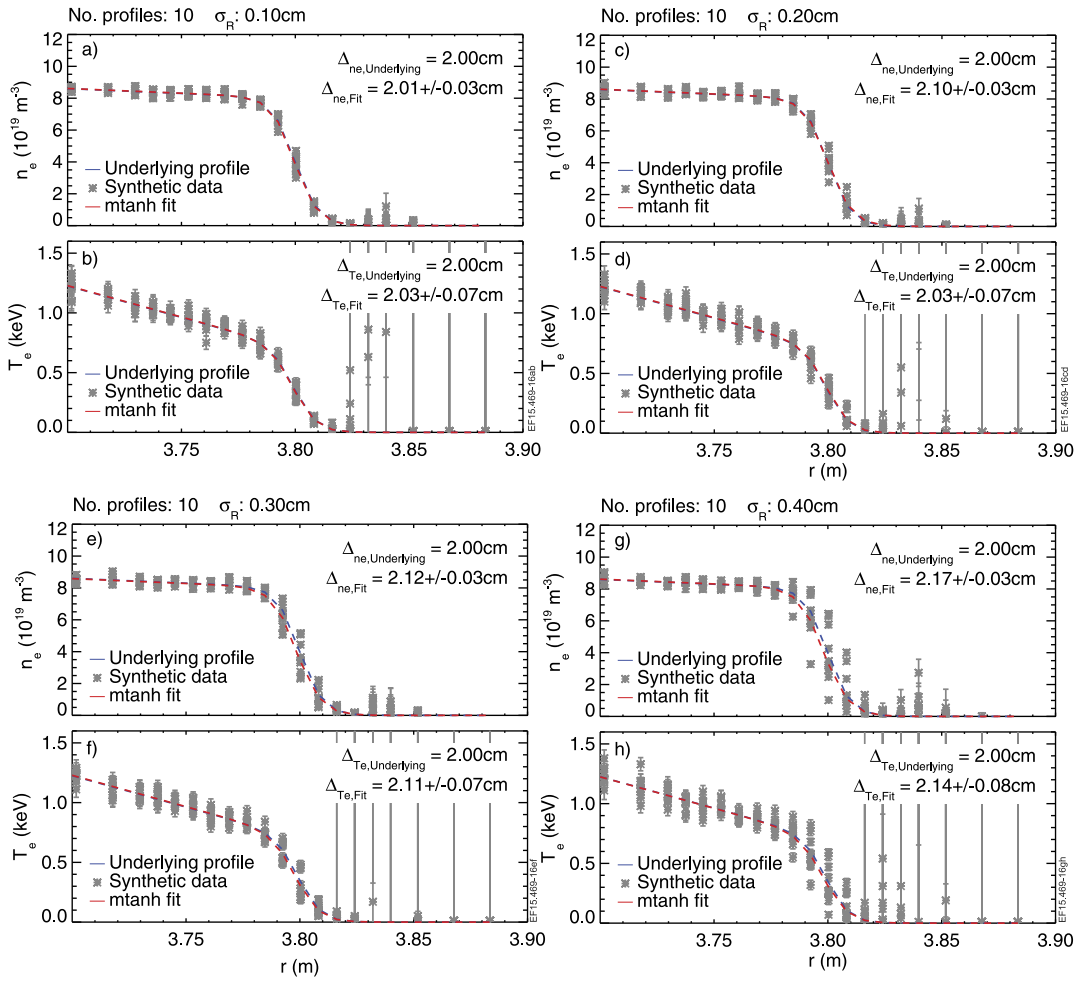

FIG. 16. Underlying mtanh profile (blue), synthetic data (grey), and mtanh fit to a composite of 10 synthetic profiles (blue). The random error is sampled from a normal distribution of width (a) and (b) $\sigma_R = 0.1$ cm, (c) and (d) $\sigma_R = 0.2$ cm, (e) and (f) $\sigma_R = 0.3$ cm, and (g) and (h) $\sigma_R = 0.1$ cm.

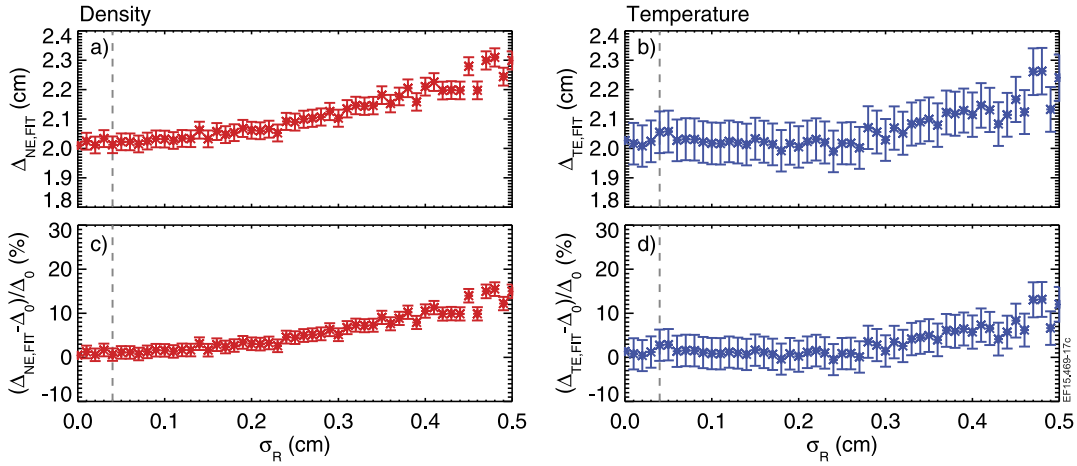

FIG. 17. Scan of σ_R ranging from 0.0 cm to 0.5 cm for (a) temperature pedestal width, (b) density pedestal width, (c) percentage error in temperature pedestal width, and (d) percentage error in density pedestal width as determined by fitting to composite profile (Fig. 15 consisting of HRTS like profiles, see Section III).

the temperature and density by repeating this minimisation process 100 times for different synthetic signals, as varied according to the random error, and taking the standard deviation.

D. Example synthetic HRTS profiles

Figures 13 and 14 show an example of radial synthetic profiles along the magnetic mid-plane. The pre-ELM pedestal fit for JET pulse number 82585 is taken as the underlying profile. The cold transmission curve for both the upper and lower lines-of-sight mapped onto the magnetic mid plane (as shown in Figure 3) is incorporated into the calculation of the number of photons for the profiles shown in Figures 13 and 14, respectively. Both the upper and lower lines-of-sight demonstrate the difference vignetting has on the synthetic profiles. For both Figs. 13 and 14, panels (a) and (c) show the entire extend of the synthetic profile, while panels (b) and (d) focus on the pedestal region.

In the SOL region of a plasma, the temperature and density are at the limit of the dynamic range of the HRTS diagnostic as the system suffers from a low number of detected photons. In other words, the detected number of photons falls below the background and amplifier photon error. Consequently, in this instance, the fitted temperature and density is a reflection of the random noise and not the detected signal. This effect results in a rapid increase in the uncertainty within the SOL of the orders $\sigma_{Te} \approx 3$ keV and $\sigma_{Te} \approx 1 \times 10^{19}$ m^{-3}.

Comparison of Figures 13 and 14 demonstrates that the rapid increase in uncertainty occurs at R ≈ 3.82 m for the lower line of sight in comparison to R ≈ 3.81 m for the upper line of sight. The upper line of sight compromises one to two spatial points relative to the lower line of sight.

IV. QUANTIFYING THE SYSTEMATIC ERROR DUE TO ELM SYNCHRONISATION

This section quantifies the systematic error introduced due to the radial shift when overlaying the JET HRTS profiles. The profiles are shifted according to the last closed flux surface (LCFS) as determined by the magnetic equilibrium. This is to account for small scale fluctuations in plasma position and any error in the position of the last closed flux surface. It is inconsequential whether this uncertainty in profile position is a real movement of the plasma or an artifact of the magnetic equilibrium reconstruction as what is important is to accurately overlay the steep gradient region of the profiles.

Figure 15 shows a schematic diagram describing the method used to assess the systematic uncertainty in the radial shift. There are three steps: (1) an underlying profile is defined (grey), (2) a composite profile is generated (blue) by overlaying multiple HRTS like profiles with different pedestal positions (the error on the pedestal position is sampled from a normal distribution), and (3) a mtanh is fitted to the composite profile. The difference between the fitted and the original underlying parameters is then assessed.

Figure 16 shows the fit to a composite of 10 synthetic temperature and density HRTS profiles, which incorporate the vignetting curve for the lower line of sight for (a) and

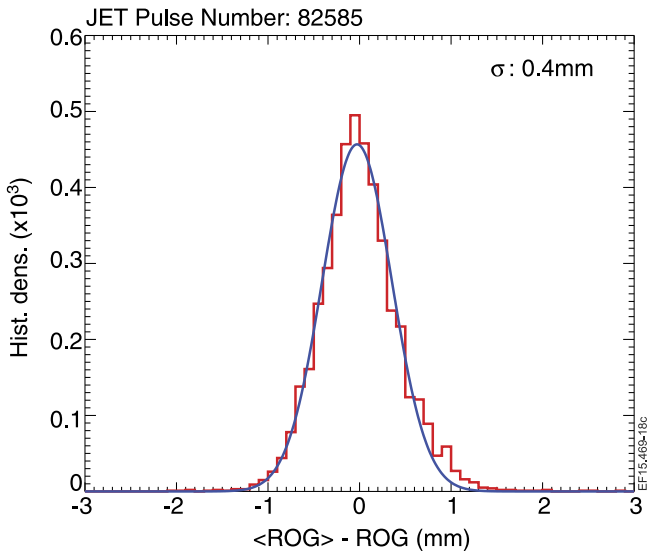

FIG. 18. Histogram of the difference between the un-smoothed and smoothed Radial Outer Gaps (ROGs) as a function of time (red) and a corresponding gaussian fit (blue).

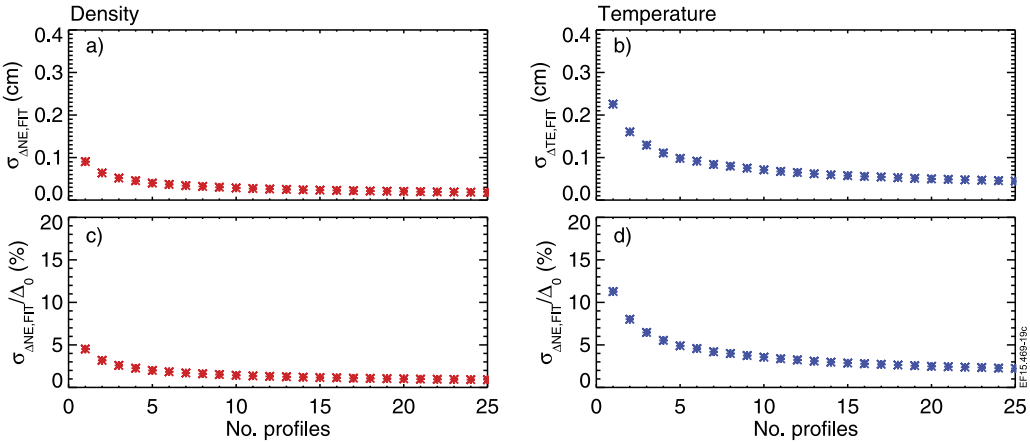

FIG. 19. Variation in pedestal width for (a) temperature and (b) density. Percentage error in pedestal width for (c) temperature and (d) density as determined from mtanh fits to a composite profile where $\sigma_R = 0.4$ cm.

(b) $\sigma_R = 0.1$ cm, (c) and (d) $\sigma_R = 0.2$ cm, (e) and (f) $\sigma_R = 0.3$ cm, and (g) and (h) $\sigma_R = 0.4$ cm. The error bars on the temperature and density points above R ≈ 3.81 m are large in comparison to the measured value. Figures 16(a) and 16(b) show that the density and temperature pedestal widths are accurately recovered within the statistical error. However, as σ_R increases (for example, consider Figures 16(g) and 16(h) where $\sigma_R = 0.4$ cm), the fitted width systematically deviates from the underlying width beyond the statistical error.

Figure 17 shows the average systematic deviation over 20 Monte-Carlo runs of the temperature and density pedestal widths over a scan of σ_R from 0.0 to 0.5 cm. For a composite profile consisting of 10 synthetic profiles, the systematic deviation in pedestal width increases with σ_R for both the temperature and density. The systematic error is the deviation from the underlying width outside the statistical error. For small σ_R (<0.2 cm), the systematic error is negligible in comparison to the statistical error. At high σ_R (>0.3 cm), the systematic deviation becomes significant.

The LCFS position, used to correct the radial position of the real HRTS profiles when forming the composite profile, is calculated using the high time resolution magnetic reconstruction. The Radial Outer Gap (ROG), which is the distance between the plasma edge and wall, is converted into the LCFS position using geometric information. The ROG can be used to quantify the variation in position by smoothing the time trace and evaluating the residuals. Figure 18 shows a histogram of the residuals during the inter-ELM stationary phase (excluding the ELM crash; the rapid collapse of the steep pressure gradient resulting in the loss of energy and particles) of a JET-ILW pulse along with a corresponding Gaussian fit. The width of this Gaussian is $\sigma_R = 0.4$ cm, an estimate of the uncertainty in profile position for real HRTS measurements.

The vertical lines in Figure 17 show how the experimental estimate for σ_R relates to the scan of σ_R. Assuming $\sigma_R \approx 0.4$ cm and the composite profile consists of 10 profiles, the expected systematic error is found to be negligible for both the density and temperature pedestal widths in comparison to the corresponding statistical error.

It is important to be aware that the absolute value of the systematic error is sensitive to the photon error on each channel. More specifically, it could be argued that the photon errors for the channels closest to the laser wavelength are unrealistically small (Figure 12). Consequently, the temperature and density errors would be uncharacteristically small, particularly, at the lower limit of the diagnostic dynamic range (pedestal foot). If the photon error was artificially increased, the statistical and systematic errors on the pedestal width would also increase. Yet, it can be shown that the systematic error would still increase with σ_R and for JET ELM synchronised fits ($\sigma_R \approx 0.4$ cm), the systematic error on the pedestal width would still be negligible in comparison to the statistical error.

The method described in Figure 15 can be adapted to investigate how the statistical error varies with the number of profiles within the composite profile. Figure 19 shows how the statistical error (in cm and as a percentage of the underlying temperature and density pedestal widths) varies with the number of profiles in the composite profile. The value of σ_R is fixed at 0.4 cm. The statistical error is large (±5% for density and 12% for temperature) for one profile but reduces as the number of profiles increases. As described above, it is noted the statistical error for the pedestal width is sensitive to the photon errors on each channel. Nevertheless, the reduction in statistical error with increasing number of profiles would still be observed. Figure 19 shows the reduction in the statistical error on the pedestal width begins to plateaus at five profiles. Consequently, this should be considered as a minimum number of profiles required for a fit, which typically equates to a stationary ELMy phase of 1.5–2.0 s.

V. CONCLUSIONS

The JET pedestal structure is quantified by performing a mtanh fit to ELM synchronised electron temperature and density profiles. In addition to statistical error, systematic errors also contribute to the total error associated with the mtanh parameters. The systematic error due to the deconvolution technique, which incorporates the HRTS instrument function, has been previously quantified. This paper presents a simulation, using synthetic JET HRTS-like profiles, that

quantifies the systematic error due to ELM synchronisation on the pedestal width.

In the context of this paper, a synthetic HRTS-like profile is as a profile, generated from an underlying profile, with error bars and point-to-point variation characteristic of the JET HRTS system. To generate such a profile, first, the photon throughput of the HRTS system is estimated, approximating the system transmission losses and comparing this to the number of photons collected during the Raman calibration (which offers a continuous stable measurement of known density). The measured number of Raman scattered photons, as determined by the signal-to-noise ratio, is found to be within a factor of 0.52 (core) and 0.31 (edge), with good agreement in the radial profile shape. By correcting the number of Thomson scattered photons for a given temperature and density by 0.52 (core) or 0.31 (edge) and comparing with the Thomson scattered wavelength distribution, given by the Selden-Naito expression at a given temperature, the number of photons in each spectral channel can be accurately evaluated. The synthetic measured temperature and density are then determined by fitting to the response of each channel incorporating errors from photon noise (Poisson statistics) in addition to the amplifier and background light noise. The spread of temperature and density measurements when performing the fit numerous times is used as the corresponding overall error in the fit. Analysis of the effect of vignetting for the two possible HRTS lines-of-sight shows that there is a degradation of measurement quality for two more edge spatial points on the upper line-of-sight.

A Monte Carlo simulation that replicates the fitting technique to ten synthetic HRTS-like profiles demonstrates that the systematic error due to ELM synchronisation is negligible in comparison to the statistical uncertainty, for the assumptions made when generating the profiles and in the subsequent simulation. The number of synthetic profiles, ten, is the typical number of selected profiles for a JET pre-ELM (70%-99%) fit over a stationary phase of 1.5-2.0 s. In addition, this simulation has been adapted to show that, with increasing number of profiles, the statistical error reduces and plateaus at five, which should be considered a minimum number of profiles for a fit.

ACKNOWLEDGMENTS

This work has been carried out within the framework of the EUROfusion consortium and has received funding from the Euratom research and training programme 2014-2018 under Grant Agreement No. 633053. The views and opinions expressed, herein, do not necessarily reflect those of the European Commission.

[1]F. Wagner *et al.*, "Regime of improved confinement and high beta in neutral-beam-heated divertor discharges of the ASDEX tokamak," Phys. Rev. Lett. **49**, 1408 (1982).
[2]H. Zohm *et al.*, "Edge localized modes (ELMs)," Plasma Phys. Control. Fusion **38**, 105–128 (1996).
[3]J. W. Connor *et al.*, "Magnetohydrodynamic stability of tokamak edge plasmas," Phys. Plasmas **5**, 2687 (1998).
[4]R. Pasqualotto *et al.*, "High resolution Thomson scattering for Joint European Torus (JET)," Rev. Sci. Instrum. **75**, 3891–3893 (2004).
[5]L. Frassinetti *et al.*, "Spatial resolution of the JET Thomson scattering system," Rev. Sci. Instrum. **83**, 013506 (2012).
[6]M. N. A. Beurskens *et al.*, "Pedestal width and ELM size identity studies in JET and DIII-D; implications for ITER," Plasma Phys. Control. Fusion **51**, 124051 (2009).
[7]M. N. A. Beurskens *et al.*, "H-mode pedestal scaling in DIII-D, ASDEX Upgrade, and JET," Phys. Plasmas **18**, 056120 (2011).
[8]M. N. A. Beurskens *et al.*, "The effect of metal wall on confinement in JET and ASDEX Upgrade," Nucl. Fusion **55**, 124043 (2013).
[9]M. J. Leyland *et al.*, "Pedestal study across a deuterium fuelling scan for high δ ELMy H-mode plasmas on JET with the carbon wall," Nucl. Fusion **53**, 083028 (2013).
[10]M. J. Leyland *et al.*, "The H-mode pedestal structure and its role on confinement in JET with a carbon and metal wall," Nucl. Fusion **55**, 013019 (2015).
[11]R. J. Groebner *et al.*, "Critical edge parameters for H-mode transition in DIII-D," Plasma Phys. Control. Fusion **40**, 673–677 (1998).
[12]P. A. Schneider, "Differences in the H-mode pedestal width of temperature and density," Plasma Phys. Control. Fusion **54**, 105009 (2012).
[13]C. F. Maggi *et al.*, "Pedestal and core confinement of hybrid scenario in ASDEX Upgrade and DIII-D," Nucl. Fusion **50**, 025023 (2010).
[14]R. J. Groebner *et al.*, "Temporal evolution of H-mode pedestal in DIII-D," Nucl. Fusion **49**, 045013 (2009).
[15]R. J. Groebner *et al.*, "Limits to the H-mode pedestal pressure gradient in DIII-D," Nucl. Fusion **50**, 064002 (2010).
[16]J. W. Hughes *et al.*, "H-mode pedestal and L-H transitions studies on Alcator C-Mod," Fusion Sci. Technol. **51**, 317–341 (2007).
[17]A. E. Hubbard *et al.*, "Pedestal profiles and fluctuations in C-Mod enhanced D-alpha H-modes," Phys. Plasmas **8**, 5 (2001).
[18]A. Kirk *et al.*, "A comparison of H-mode pedestal characteristics in MAST as a function of magnetic configuration and ELM type," Plasma Phys. Control. Fusion **51**, 065016 (2009).
[19]D. Dickinson *et al.*, "Towards the construction of a model to describe the inter-ELM evolution of the pedestal on MAST," Plasma Phys. Control. Fusion **53**, 115010 (2011).
[20]D. Dickinson *et al.*, "Kinetic instabilities that limit b in the edge of a tokamak plasma, a picture of an H-mode pedestal," Phys. Rev. Lett. **108**, 135002 (2012).
[21]A. Kirk *et al.*, "Evolution of the pedestal on MAST and the implications for ELM power loadings," Plasma Phys. Control. Fusion **49**, 1259–1275 (2007).
[22]A. Diallo *et al.*, "Dynamical evolution of pedestal parameters in ELMy H-mode in the national spherical torus experiment," Nucl. Fusion **51**, 103031 (2011).
[23]T. Hatae *et al.*, "Understanding of H-mode pedestal characteristics using the multimachine pedestal database," Nucl. Fusion **41**, 3 (2001).
[24]R. Scannell *et al.*, "Deconvolution of Thomson scattering temperature profiles," Rev. Sci. Instrum. **85**, 053501 (2011).
[25]H. Salzmann *et al.*, "The LIDAR Thomson scattering diagnostic on JET," Rev. Sci. Instrum. **59**, 8 (1988).
[26]M. Brix *et al.*, "Upgrade of the lithium beam diagnostic at JET," Rev. Sci. Instrum. **88**, 10D733 (2010).
[27]A. Sirinelli, "Multiband reflectrometry system for density profile measurement with high temporal resolution on JET tokamak," Rev. Sci. Instrum. **81**, 10D939 (2010).
[28]E. de la Luna *et al.*, "Electron cyclotron emission radiometer upgrade on the Joint European Torus (JET) tokamak," Rev. Sci. Instrum. **75**, 3831 (2004).
[29]A. C. Selden, "Simple analytic form of the relativistic Thomson scattering spectrum," Phys. Lett. A **79**(5-6), 405 (1980).
[30]M. N. A. Beurskens *et al.*, "Error analysis of Rijnhuizen tokamak project Thomson scattering data," Rev. Sci. Instrum. **70**, 1999–2011 (1999).
[31]R. Scannell, "Investigation of H-mode edge profile behaviour on MAST using Thomson scattering," Ph.D. thesis, University College Cork, 2007.
[32]J. Flanagan *et al.*, "Alternative calibration techniques for Thomson scattering diagnostics on large fusion devices via an integrated data approach," in *IOP Plasma Physics Conference*, 2010.
[33]T. O'Gorman, "Investigation of neoclassical tearing modes on MAST using Thomson scattering,,"' Ph.D. thesis, University College Cork, 2012.